ARTICLE

Stoichiometrically Optimized e_g Orbital Occupancy of Ni-Co Oxide Catalysts for Li-Air Batteries

Received 00th January 20xx,
Accepted 00th January 20xx

DOI: 10.1039/x0xx00000x

Shadeepa Karunarathne[a], Yasun Y. Kannangara[b], Chirag R. Ratwani[a], Chanaka Sandaruwan[b], W.P.S.L. Wijesinghe[b], Ali Reza Kamali[c,d], Amr M. Abdelkader[a†]

Li-air battery (LAB) technology is making continuous progress toward its theoretical capacity comparable to gasoline. However, the sluggish reaction at the cathode is still a challenge. We propose a simple strategy to optimize the surface, e.g. occupancy, by adjusting the stoichiometric ratios of transition metal-based spinel structures through a controlled hydrothermal synthesis. Three distinct stoichiometries of Ni-Co oxides were used to demonstrate the direct correlation between the stoichiometry and the catalytic performances. The groundsel flower-like structure having 1: 1.4 Ni: Co atomic ratio with high surface area, high defect density, and the abundance of Ni^{3+} at the surface with semi-filled e_g orbitals was found to benefit the structure promoting high catalytic activities in aqueous and aprotic mediums. The assembled LAB cells employing this cathode demonstrate an exceptional lifespan, operating for 3,460 hours and completing 173 cycles while achieving the highest discharge capacity of 13,759 $mAhg^{-1}$ and low charging overpotentials. The key to this prolonged performance lies in the full reversibility of the cell, attributed to its excellent OER performance. A well-surface adsorbed, amorphous LiO_2/ Li_2O_2 discharge product is found to possess high diffusivity and ease of decomposition, contributing significantly to the enhanced longevity of the cell.

Keywords: Li-Air batteries, stoichiometric optimization, e_g orbital occupancy, binary oxide catalysts

a Faculty of Science and Technology, Bournemouth University, Talbot Campus, Poole, BH12 5BB, UK
b Sri Lanka Institute of Nanotechnology, Pitipana, Homagama, Sri Lanka
c School of Metallurgy, Northeastern University, Shenyang, 110819, China
d Department of Materials Science and Metallurgy, University of Cambridge, Cambridge
† Corresponding authors: Dr Amr M. Abdelkader (aabdelkader@bournemouth.ac.uk)
Electronic Supplementary Information (ESI) available: [details of any supplementary information available should be included here]. See DOI: 10.1039/x0xx00000x

Introduction

High-density renewable energy storage is becoming increasingly important due to the limited availability of fossil fuels and the global demand for renewable energy sources.[1,2] Metal-air battery technology is a promising sustainable green energy storage alternative consisting of a metallic anode (e.g., Li, K, Na, Zn, Fe, and Al), a porous cathode, and a compatible electrolyte.[3] Aprotic Li-Air batteries (LABs) are considered the best possible alternative since they offer the highest possible theoretical energy density (11.4 kWh kg^{-1}) and specific capacity (1170Ah kg^{-1}).[4] A successful LAB is yet to be commercialized owing to its sluggish air cathode reaction kinetics and related parasitic reactions associated with oxygen reduction reaction (ORR) and oxygen evolution reaction (OER) occurring during the discharging and charging steps, respectively.[5] These sluggish kinetics and parasitic reactions lead to fast decay in battery performance by accumulating undecomposed discharged products at the cathode surface. [6,7]

A better-performing bifunctional catalyst should help the LAB sustain many cycles with low overpotential and high efficiency by promoting oxygen kinetics and controlling the discharged product morphology.[8] In recent years, enormous efforts have been made to develop suitable bifunctional catalysts that could be incorporated into the cathode architecture. Noble metals remain at the top of the list of high-performing catalysts. [9,10] However, excessive costs limit the practical usage of noble metals and their derivatives in LABs.[11] Numerous low-cost alternatives have shown promising results, such as doped/ undoped carbon [12] and derivatives of non-precious transition metals, including its oxides,[13] and sulfides.[14] Despite their decent ORR activity owing to their suitable pore structure and high conductivity, carbonaceous materials were found to be susceptible to reduced oxygen compounds (ROC) and singlet oxygen ($^1O_2$) generated during the charging cycle, and Gallant et al. observed all the carbon cathode surface oxidizes forming insulating Li_2CO_3 as it reacts with Li_2O_2 present at proximity.[15] Since potentials over 3.82 V are needed to decompose Li_2CO_3, higher charging overpotentials are needed during the OER, leading to further cell decomposition as it is exposed to higher active ROS and singlet oxygen.[16] The current search is to find alternative stable cathode materials. Transition metal oxides (TMOs) have demonstrated encouraging performances in the last few years, specifically due to their high stability during OER [17], motivating further research in the field.[18] Among many TMOs explored, binary spinel structures like $CoFe_2O_4$, [18] and $NiFe_2O_4$ [19] produced decent bifunctional activity for Li-air batteries, where the mixed valences in AB_2O_4 spinel structures contribute to enhancing the catalytic activity and obtaining good electrical conductivity, overcoming the inherent insulative nature of TMOs.[20] In particular, $NiCo_2O_4$ has gained considerable attention due to its excellent electrochemical properties. [21]

Nevertheless, the high intrinsic resistivity and the limited catalytic activity of TMOs limit their performances as a long-lasting stable catalyst, and using carbon-rich highly resistive binders further amplifies the instability as commonly using binders such as PVDF, PAN, PVC, and PVP was found to be unstable to Li_2O_2 [22]; hence, binder-free cathodes were preferred.[23] Further, recently, it was identified that the catalytic activity in transition metal-based catalysts could be enhanced by tuning the, e.g. orbital occupation, where a low occupancy in, e.g. orbit with a higher number of unsaturated coordination cations is found to be forming a strong bonding between reaction intermediates, improving the oxygen reaction kinetics. Different orbital engineering and facet engineering techniques, such as alloying 24, doping 25, selective facet growth 26, and forming heterostructures 27, were found to be successful up to date in altering the orbital occupancy in transition metal-based catalysts used in LABs.

Important parameters that have yet to receive adequate attention in the existing literature pertain to the impact of the spinel binary oxide stoichiometry, the associated stoichiometric defects towards the electronic properties of the catalyst, and its effects on the electrode's electrochemical performance. In this research, we explore this gap by producing three distinct Ni-Co oxide stoichiometries with dissimilar morphological features, achieved through precise control of nucleation and crystal growth during hydrothermal conditions. Amongst the tested structures, interestingly, the defect-rich inverted spinel structure, formed into a hierarchical groundsel flower-like microstructure directly anchored on the fur-like surface grown on the Ni foam, yielded the best catalytic activity. This structure, having a 1.38 Ni: Co stoichiometry and high Ni^{3+}/Ni^{2+} and Co^{2+}/Co^{3+} ratios, with plentiful unsaturated coordination cations exhibited exceptional OER and ORR performances in both aqueous and aprotic mediums, with only 1.56 V to reach 10 mA cm^{-2} current density and a halfwave potential of 0.89 V in the respective OER and ORR studies in the aqueous medium. Additionally, it displayed an excellent Li-air battery performance, boasting a specific discharge capacity of 13759 $mAhg^{-1}$ and a remarkable cyclability of 173 cycles, further demonstrating the key attributes by the synthesized porous binary oxide 3D network with favourable e_g orbital occupation, stoichiometry, and facets supporting fast oxygen redox kinetics and large depositions of the discharged product. Further analysis

into the discharged and recharged electrodes found that the high diffusivity and the easy decomposability of the formed amorphous discharge product helped the efficient and durable cyclability of the battery, while the resistance shown by the binder-free binary oxide cathode against the parasitic reaction involving ROC and singlet oxygen helped the sustainable operation with full recovery. These findings highlight the importance of the study, providing deeper insight into optimizing the stoichiometry of binary oxides to obtain favourable e_g orbital occupation for enhanced Li-air battery operation.

Experimental Section

Synthesis of in-situ electrocatalyst-loaded electrodes

The electrocatalysts of $NiCo_2O_4$ were directly grown on the surface of a Ni foam using a hydrothermal method. In a typical synthesis, 2.5 mmol Ni $(NO_3)_2{\cdot}6H_2O$, 5 mmol of Co $(NO_3)_2{\cdot}6H_2O$, and 10 mmol of urea were dissolved into 100 ml deionized water, and 70 ml of it transferred into a 100 ml Teflon-lined stainless steel autoclave vessel. The surface of the Ni foam was prepared suitable for catalyst growth by degreasing the surface via ultrasonic cleaning in an ethanol/ DI (deionized) water mixture, followed by etching out the surface oxide layer using diluted HCl and HNO_3 acid solutions. A 5×2 cm well-cleaned freshly prepared Ni foam was vertically immersed in the precursor-filled autoclave vessel, and it heated at 5 ^{0}C min^{-1} before maintaining at 120 ^{0}C for 12 h. After letting the autoclave vessel cool down to room temperature, the catalyst-coated Ni foams were collected and washed thoroughly with DI water before air drying at 60 ^{0}C for 12 hours. The dried samples were calcined for 4 hours at 400 ^{0}C with a ramping rate of 5 ^{0}C min^{-1} in the air to obtain the final product of NCO 120, which was found to be loaded with catalyst material ~0.8 mg cm^{-2}. For comparison, two other catalysts were synthesized under different thermodynamic environments by maintaining the autoclave at 150 ^{0}C (NCO 150) and 180 ^{0}C (NCO180) for 12 hours, respectively, as shown in Fig. S1 while keeping the other parameters the same.

Material Characterization

Crystalline phases of synthesized materials were identified using X-ray powder diffraction (XRD) on a Siemens D5000 diffractometer with Cu K_α radiation (Siemens, Germany). The morphology of the synthesized $NiCo_2O_4$ catalysts was examined using scanning electron microscopy (SEM, HITACHI SU6600), and the microstructure and crystallinity of samples were further examined using transition electron microscopy (TEM, JEOL JEM-2100) combined with selected area electron diffraction (SAED) and inverse- fast Fourier transform (FFT). Brunauer–Emmett–Teller (BET) surface area was measured using N_2 adsorption/desorption at 77.3 K on an Autosorb iQ Station 1 after the samples were degassed at 150 ^{0}C for 12 h under vacuum before physisorption measurements. X-ray photoelectron Spectroscopy (XPS) was performed using ESCALB 250Xi spectrophotometer (Thermo Fisher, USA). Al kα radiation was used with the spot size of 900 µm with the monitored beam values of 14.4 kV (Anode HT), and 18.08 mA (Beam current). All XPS measurements were performed in constant analyzer energy (CAE) mode and 2000 eV of ion energy with the mid-range current used for 30 seconds to clean the surface.

Electrochemical Measurements

The OER and ORR performances of the as-prepared in-situ coated electrocatalysts were evaluated using a three-electrode setup attached to the IviumStat system, where the catalyst grafted Ni foam were used as the working electrode while Pt foil and saturated calomel electrodes were used as counter and reference electrodes respectively. 1 M KOH electrolyte was used as the electrolyte, and all the measured potentials were transformed at RHE following the formula of $E_{(RHE)} = E_{(SCE)} + 0.241 + 0.059*pH$. The working electrodes were activated through cyclic voltammetry (CV) tests at 100 mVs^{-1} before CV and linear sweep voltammetry (LSV) measurements. The OER LSV measurements were carried out at a rate of 10 mV s^{-1} in a saturated Ar atmosphere, while ORR LSV polarisation curves were recorded at a scan rate of 5 mV s^{-1} with rotation rates ranging from 0 to 1500 rpm in a saturated O_2 environment. Electrochemical impedance spectroscopy (EIS) was performed for the frequency range of 1 MHz to 0.01 Hz with a 5 mV sinusoidal signal. Further, the catalyst's long-term stability was studied with chronopotentiometric measurements with a current density of 10 mA cm^{-2}.

The Li-air battery CR-2032 type meshed coin cells were assembled in an Ar-filled glovebox, where 13 mm disks of 0.5- 0.8 mg cm^{-2} catalyst loaded Ni foam was used as the battery cathode while 1 mm thick Li foil, celgard 2500 membrane, and 1 M LiTFSI in tetraethylene glycol dimethyl ether (TEGDME) solution were used as the anode, separator, and the electrolyte respectively. Assembled batteries were kept in a sealed dry air environment at 1 atm for 5 h before electrochemical analysis. CV analysis for Li-air cell was conducted at 2.0-4.5 V Vs Li/Li^+ potential window with 0.5 mV s^{-1} using IviumStat system, and galvanostatic discharge/charge analysis was performed using a Neware battery analyzer where the specific capacities and current densities were calculated considering the amount of active material

present in the battery cathode. EIS, SEM, and Raman microscopy techniques were utilized for discharge product analysis.

Results and Discussion

Material characterization

The Ni-Co oxide catalyst nanostructures were in-situ grafted on the Ni foam using the hydrothermal technique. The synthesis technique is known to produce non-stoichiometric hydroxide structures with crystal imperfections[28] mostly in terms of substitutional disorder (atoms in the given site are replaced by another atom) leading to the occurrence of point defects or extended defects in the calcined binary oxide nano-crystalline structure. Hence, the process helped to optimize the stoichiometry of the derived Ni-Co oxide spinel structure, forming a favourable electronic structure for faster oxygen kinetics.

Scanning electron microscopy (SEM) images identified differently synthesized NCOs' distinct morphological and structural features. Figure 1 (a)-(d) indicates that the NCO 120 structure has well-interconnected groundsel flower-like 3D morphology directly anchored on the Ni foam, and the remaining surface of the Ni foam is well covered with fur-like grown $NiCo_2O_4$ as depicted in Figure 1 (d). Further, SEM images of NCO 120 in Figure 1 (b, c) and the histogram presented in Figure S2 verify the hierarchical growth nature of catalyst microstructures on the Ni foam with a narrow particle size distribution (5.28 ± 1.19 µm), in addition to the identified petal diameter of ~30 nm (see Figure 1 (c)). This hierarchical structure can provide a high surface area to exploit many exposed active sites and simultaneously leave enough voids for improved O_2/air diffusion. Figure 1(c) further indicates that the given reaction parameters promote the unidirectional growth of the crystal to form the final groundsel flower-like structure by assembling many needle-like nanostructures. As the hydrothermal reaction temperature increased to 150 ^{0}C, it is observed that the structure of the material (NCO 150) is further opened to form a chrysanthemum flower-like morphology, as indicated in Figure 1(e), where the crystal growth seems to expand towards the second direction while keeping the well-interconnected architecture (see Figure S3). The SEM images in Figure 1(f) and Figure S4 suggest further expansion of the structure as the reaction temperature increased to 180 ^{0}C by exfoliating individual petals into lamellar-like 2D morphology, where bidirectional crystal growth is well exhibited. The modification in the morphology closely follows the dissolution-precipitation mechanism related to nucleation and crystal growth in hydrothermal synthesis.[29] The increase in crystal size, accompanied by a more open architectural structure (leading to a 2D morphology), can be attributed to the higher convection and diffusion rates resulting from elevated reaction temperatures and ramping rates in both NCO150 and NCO180. These various temperature regimes induce granular growth in different directions, allowing shifts in crystal facets and stoichiometries. EDS elemental mapping (refer to Figure 1, panels g-j) confirms the uniform presence of Ni, Co, and O within the synthesized NCO120 structure, whereas the fur-like coating and particles exhibit a comparatively lower concentration of Ni than the Ni foam.

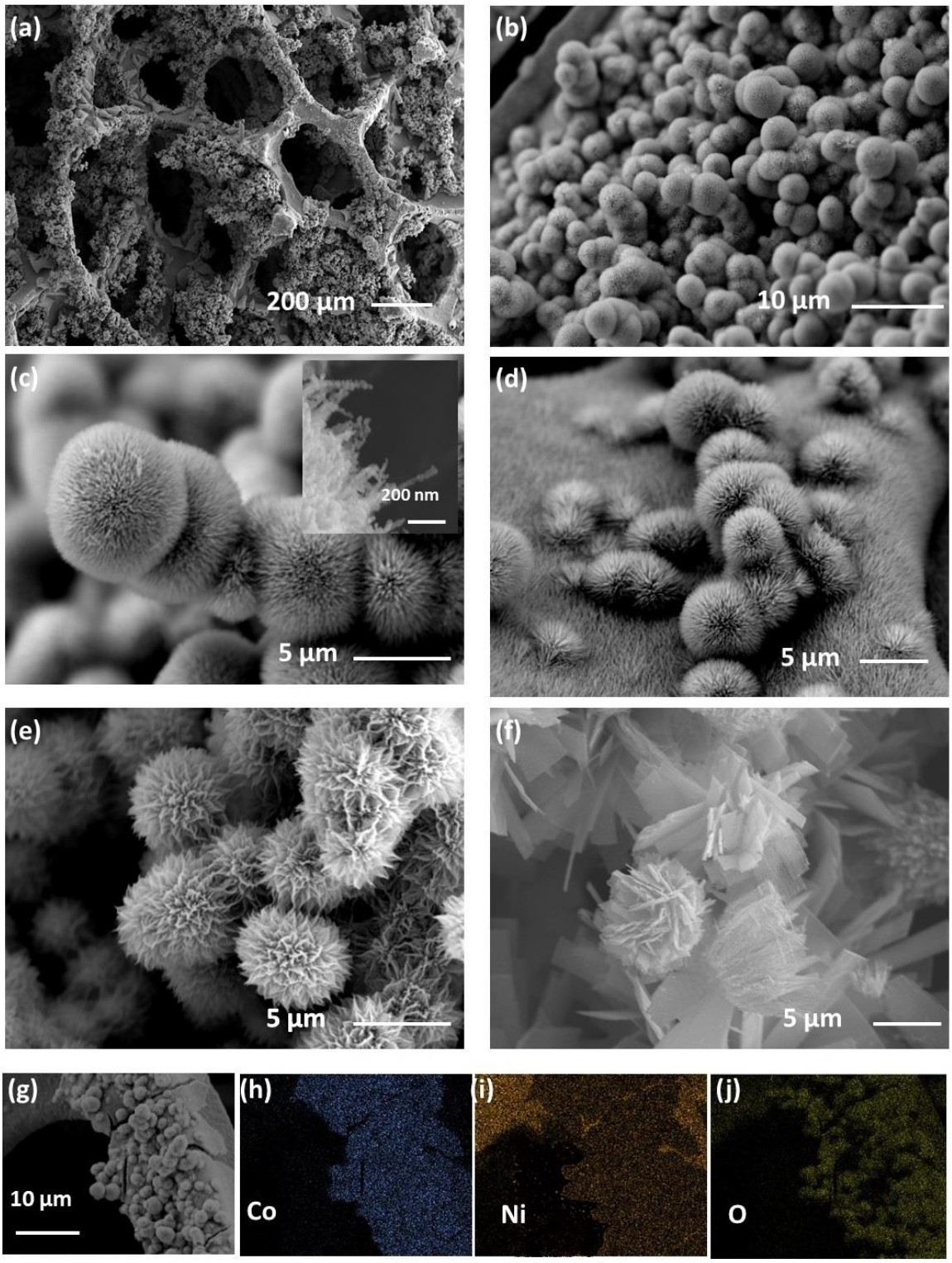

Figure 1: SEM images of different Ni-Co oxide structures anchored on Ni foam, (a-d) low and high magnifications of NCO 120 structure, (e) NCO 150, (f) NCO 180, and (g-j) EDX analysis of NCO 120 structure.

XRD patterns of various as-synthesized NCO structures were analyzed to identify their characteristic crystalline phases. The NCO powder was first detached from the Ni substrate to prevent any overlap with the diffraction signals from the substrate, as previously reported. [30] The XRD pattern in Figure 2 (a) shows that all synthesized materials have a similar nano-crystalline cubic spinel structure. The diffraction peaks presented at 2Θ = 19.0^0, 31.1^0, 36.8^0, 44.7^0, 55.5^0, 59.1^0, and 65.1^0 could be assigned to (111), (220), (311), (422), (400), (511), and (440) planes respectively, mostly agree with the typical XRD pattern for spinel cubic $NiCo_2O_4$ (JCPDS No.20-0781, a = b = c = 8.11 ^{0}A), consistent with the previous reports. [31] The other small diffraction peak in the spectrum around 43.80 is due to residual Ni from the Ni foam. It is worth noting that the XRD spectrum is more diffused for NCO 120, and much sharper diffraction peaks can be observed for NCO 180. Further, a small mismatch in the 311 peak, more distinctly with the NCO 120 structure, can be observed, and it could be due to an offset in the Ni: Co stoichiometry. The shift of the diffraction peak towards the higher angles with lower temperatures could lead to the formation of more Ni-rich compounds, possibly by replacing Co^{2+} with Ni^{3+} ions with a smaller ionic radius. Such a phenomenon aligns with the concept of the partial inversion of spinel crystal structures, where peak shifts and the decrease in intensity are related to a low crystalline material with the increased disorder[32] as the tetrahedral Co^{2+} sites exchanged with octahedral Ni^{3+}, reducing the symmetry of the structure.[33]

TEM, HR-TEM, SAED, and inverse-FFT were used to further evolute the microstructures of the NCO samples, including their morphological and crystalline lattice properties. The TEM image of an individual petal of the NCO 120 microstructure (Figure 2 (c)) shows that the petals are assemblies of small crystals of size varying from 25-40 nm in diameter. The selected-area diffraction (SAED) pattern with well-defined diffraction spots in Figure 2 (e) reveals the presence of crystalline Ni-Co oxides. In contrast, the recognized diffraction spots aligned well with the planes indexed during the XRD studies. The high-resolution TEM of the same structure identified the lattice fringes with d-spacing at about 0.24 nm and 0.47 nm, corresponding to 311 and 111 crystallographic planes of $NiCo_2O_4$, respectively (Figure 2 (d)). As indicated in the inverse-FFT analysis presented in Figure 2 (f, g), the calculated interplanar distances of 0.243 nm and 0.467 nm for respective (311) and (111) planes are marginally lower than the reported d-spacing in JCPDS No.20-0781, in agreement with the observed peak shift in the XRD analysis. The dominant surface planes of 111 and 311 are rare for $NiCo_2O_4$, providing indirect evidence of stoichiometric shifts, where the surface is known to be dominated by the 220 plane along with the (111) plane in most cases (including NCO 150 presented in Figure S5) for $NiCo_2O_4$. [34] More importantly, the image in Figure 2 (h) identifies the frequent presence of point defects (or extended defects) on the crystal facets. The defects could arise by substituting Co^{2+} ions at octahedral sites of the spinel structure with Ni^{3+} ions. In such a scenario, since the substituted Ni^{3+} ion at the octahedral site prefers to have tetrahedral coordination, the surrounding oxygen anion matrix can get distorted, and extended defects could rise by missing one or two out of six oxygen anion coordinates. The observations aligned with the previous XRD results and will be further discussed along with the XPS studies.

The characteristic N_2 adsorption-desorption isotherm curves obtained at 77.3 K for the three NCO materials are presented in Figure 2 (b). All materials present type IV isotherm H3 hysteresis behaviour with calculated BET surface areas of 62.31, 45.21, and 39.02 $m^2 g^{-1}$ for NCO 120, NCO 150, and NCO 180, respectively. Further, the NCO 120 catalyst contains a large number of mesopores with pore diameters ranging from ~ 5-30 nm with a large pore volume of 54.11 $cm^3 g^{-1}$. This mesoporous structure with higher pore volume is reported to support high discharge capacity by accommodating a large quantity of the discharged products. Also, the mesoporous structure with a higher surface area promotes full reversibility of LAB cells with lower interfacial resistance by keeping the discharged products well attached and within the structure of the cathode surface.[35]

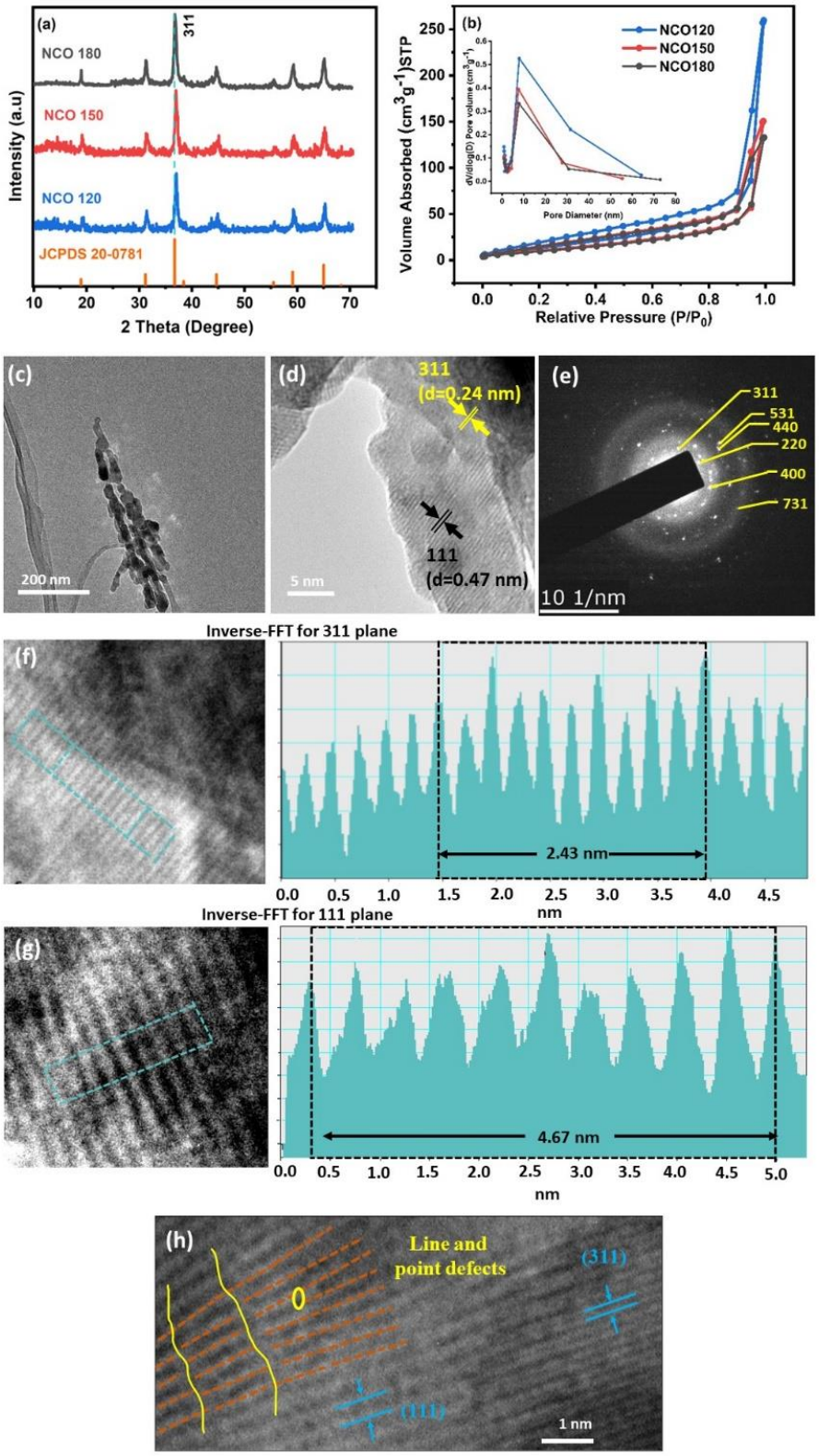

Figure 2: a) XRD patterns of the synthesized $NiCo_2O_4$ structures on Ni foam, b) Nitrogen adsorption/desorption isotherms and pore size distribution curve of $NiCo_2O_4$ structures, (c)TEM image, (d) HRTEM image, (e) corresponding SAED pattern, (f, g) inverse-FFT analysis for NCO 120 structure, and (h) crystal defects

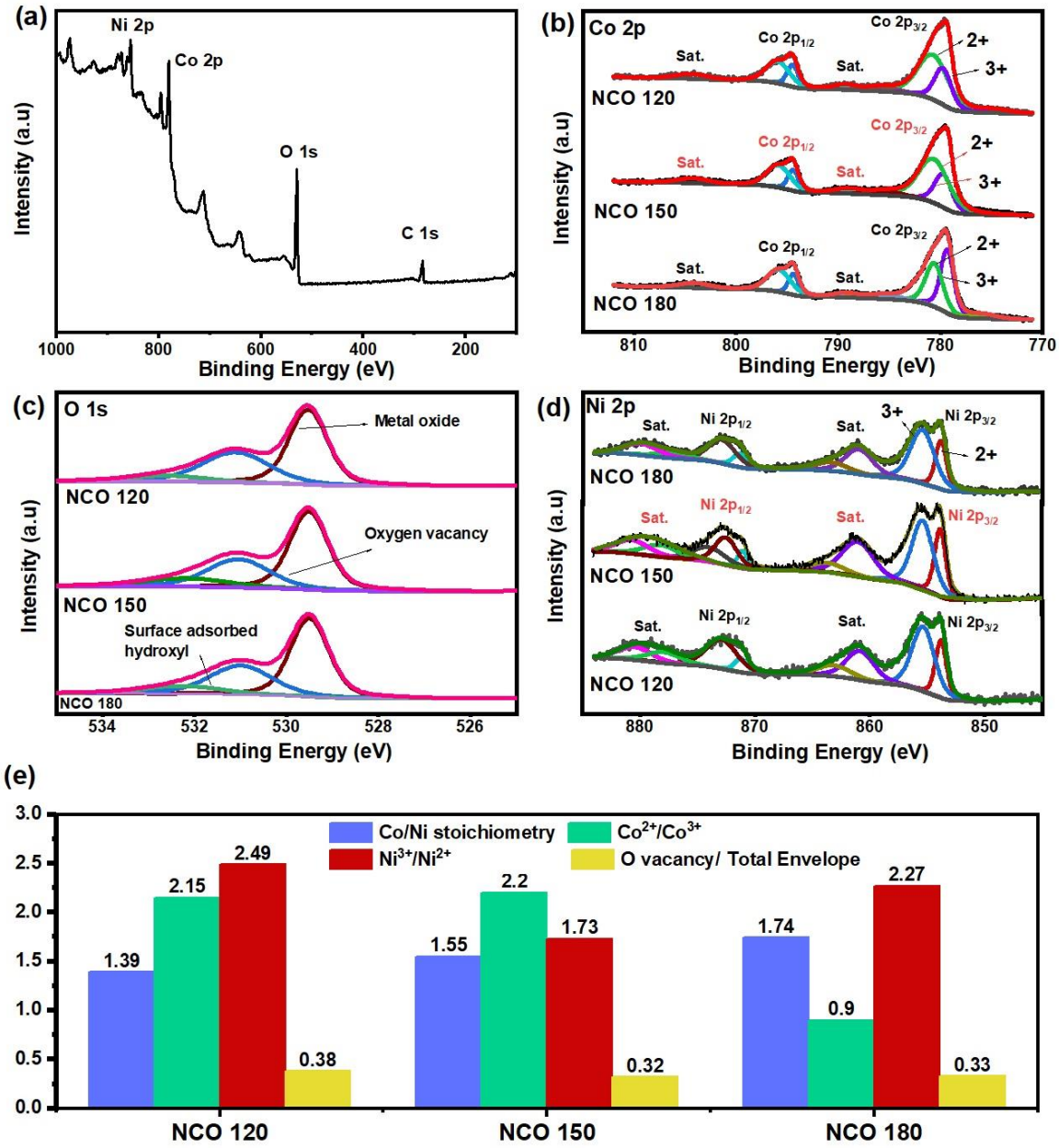

Figure. 3: XPS analysis: (a) survey spectra, (b) Co 2p spectra, (c) O 1s spectra, (d) Ni 2p spectra of as-synthesized $NiCo_2O_4$ catalysts on Ni foam, and (e) extrapolated co-relations via peak area analysis

Surface chemical states and the composition of three synthesized Ni-Co oxide catalyst materials were studied using the XPS analysis. The survey scan in Figures 3 (a) and S6 confirmed the presence of Ni, Co, and O in all three synthesized structures. As indicated in Figure 3 (b), Co 2p spectra of all three samples can be deconvoluted into well-fitted two spin-orbit doublets and shakeup satellites, where the peaks fitted at 779.7 and 794.5 eV correspond to Co^{3+} valance, while the peaks at 780.9 and 795.9 eV are assigned to Co^{2+}.[36] Similarly, the high-resolution Ni 2p spectra in Figure 3 (d) can also be fitted with two spin-orbit doubles and shakeup satellites. The peaks at 853.7 and 871.1 eV are assigned to Ni^{2+}. The peaks at 855.9 and 873.0 eV can be assigned to Ni^{3+} valance.[37] The peaks positioned at 529.5, 531.1, and 532.6 eV in O 1s spectra in Figure 3 (c) typically correspond to metal-bonded oxygen, defect sites with low oxygen coordination, and

surface adsorbed hydroxyl groups in water molecules, respectively. [38]

As Figure 3 (e) indicates, NCO 120 poses the highest amount of oxygen vacancies, corresponding to 38% of the total envelope. Further, XPS results provide evidence confirming that defects could arise by the substitution of Co^{2+} ions at octahedral sites of the spinel structure by Ni^{3+} ions, where a high Ni^{3+}/Ni^{2+} ratio and Co^{2+}/Co^{3+} ratios can be observed in the NCO 120 structure. As mentioned, the preference for tetrahedral coordinates of the substituted Ni^{3+} ions at octahedral sites, distorting the surrounding oxygen anion matrix by missing one or two out of six oxygen anion coordinates, is understood to be the mechanism of the formation of the vacancy sites. These differences in the metallic ion ratios in the derived spinel structure were achieved by altering the reaction conditions during the hydrothermal synthesis. The NCO 180 catalyst with the least substitutions and closer stoichiometry (1.74) to standard 2.0 Co/Ni stoichiometry for $NiCo_2O_4$ structure was synthesized at a relatively higher temperature of 180 ^{0}C with more favourable thermodynamic conditions, while low-temperature synthesized NCO 150 and NCO120 catalysts were found to form defect-rich non-stoichiometric complexes with respective Co/Ni stoichiometry of 1.39, and 1.55.

While knowing the identified defect sites could act as the catalyst centres promoting oxygen kinetics as previous literature suggests [39], the main objective of the current study is to understand the effect of alternation in the stoichiometry towards the catalytic activity and the battery performance. Following the concepts in molecular orbital theory, a strong interaction between the atomic orbitals of the catalyst site and the atomic orbitals of the reduced oxygen intermediates is needed to have strong adsorption of the intermediate reduced oxygen compounds ($Li_{2-x}O_2$) to the surface, facilitating a highly efficient Li-O_2 battery operation.[40] According to the crystal field theory, as the transition metals coordinate with anionic groups as oxides, the d-band splits into two energy levels, where low energy threefold (d_{xy}, $d_{yz,}$ and d_{xz}) t_{2g} base called the bonding orbitals, and the other two degenerates at a higher energy level (e_g base) called as the anti-bonding orbitals. According to Lund's rule and the Aufbau principle, electrons start to fill from the t_{2g} orbitals, and if only the bonding orbitals were filled in the catalyst site, the reduced oxygen intermediates could bond at the vacant e_g anti-bonding orbitals, making it challenging to acquire strong adsorption at scenarios where the e_g orbitals are highly occupied. Accordingly, a high catalytic activity can be expected $Ni^{3+}\left(t_{2g}{}^6 e_g{}^1\right)$ with its unsaturated e_g orbital occupation, compared to highly e_g orbital filled $Ni^{2+}\left(t_{2g}{}^6 e_g{}^2\right)$ and $Co^{2+}\left(t_{2g}{}^5 e_g{}^2\right)$ ions. Amongst the three derived Ni-Co oxides, NCO 120 presents the highest. Ni^{3+}/Ni^{2+} ratio (2.49) based on the deconvoluted peak area, compared to the ratios of 1.73 and 2.27 for NCO 150 and NCO 180 spinel structures, respectively. Hence, a high catalytic activity can be expected from the engineered NCO 120 structure with favourable e_g occupation.

Electrocatalytic activity in aqueous medium

Before constructing Li-air battery cells, the synthesised NCOs' OER and ORR catalytic activity were evaluated using a three-electrode configuration with a 1M KOH aqueous electrolyte. Figures S7(a) and (b) present the LSV polarisation curves and the associated Tafel slopes, respectively. NCO 120 possesses the lowest onset potential of 1.56 V vs RHE at 10 mA cm^{-2} current density and the smallest Tafel slope of 71 mV dec^{-1}, presenting a superior oxygen evolution activity over the other two synthesized catalysts of NCO 150 and NCO 180. In addition to the faster kinetics, the NCO 120 catalyst exhibits long-term stability, as can be concluded from the galvanostatic chronopotentiometry in Figure S8. The stability of the catalyst over 50 hours of exposure to protonated reduced oxygen species as a OH^-, $OH\cdot$, $OOH\cdot$ and O_2 verifies the stability of the catalyst against possible parasitic reactions that could occur in aprotic Li-air batteries. Following the OER assessments, the catalytic support towards ORR kinetics was also studied for all three synthesized materials. As indicated in Figure S9, all three materials draw higher reduction currents under an O_2-saturated environment, and the NCO 120 catalyst showed better activity with higher ORR current densities and peaks presenting at relatively higher potentials. The LSV curves are presented in Figure S8 (c). Again, NCO 120 exhibits the best performance with the highest onset potential of 0.94V vs RHE, the highest halfwave potential of 0.88 V, and the highest current density of 0.47 mA cm^{-2} at 0.9 V, outperforming the other two NCO catalysts. Further assessment of ORR performances can be found in the supporting information.

The experiments revealed a high Ni^{3+} atomic ratio, with NCO 120 exhibiting the highest catalytic activity, followed by NCO 180 and NCO 150 catalysts, respectively. The study further implied the significance of the conducted stoichiometric sweep in Ni-Co oxides, which could be used as a simple technique to derive high-performing electrocatalysts. Moreover, the high surface area and the binder-free, well-interconnected unique surface structure of NCO 120 may further enhance oxygen kinetics by exposing more reactive sites.

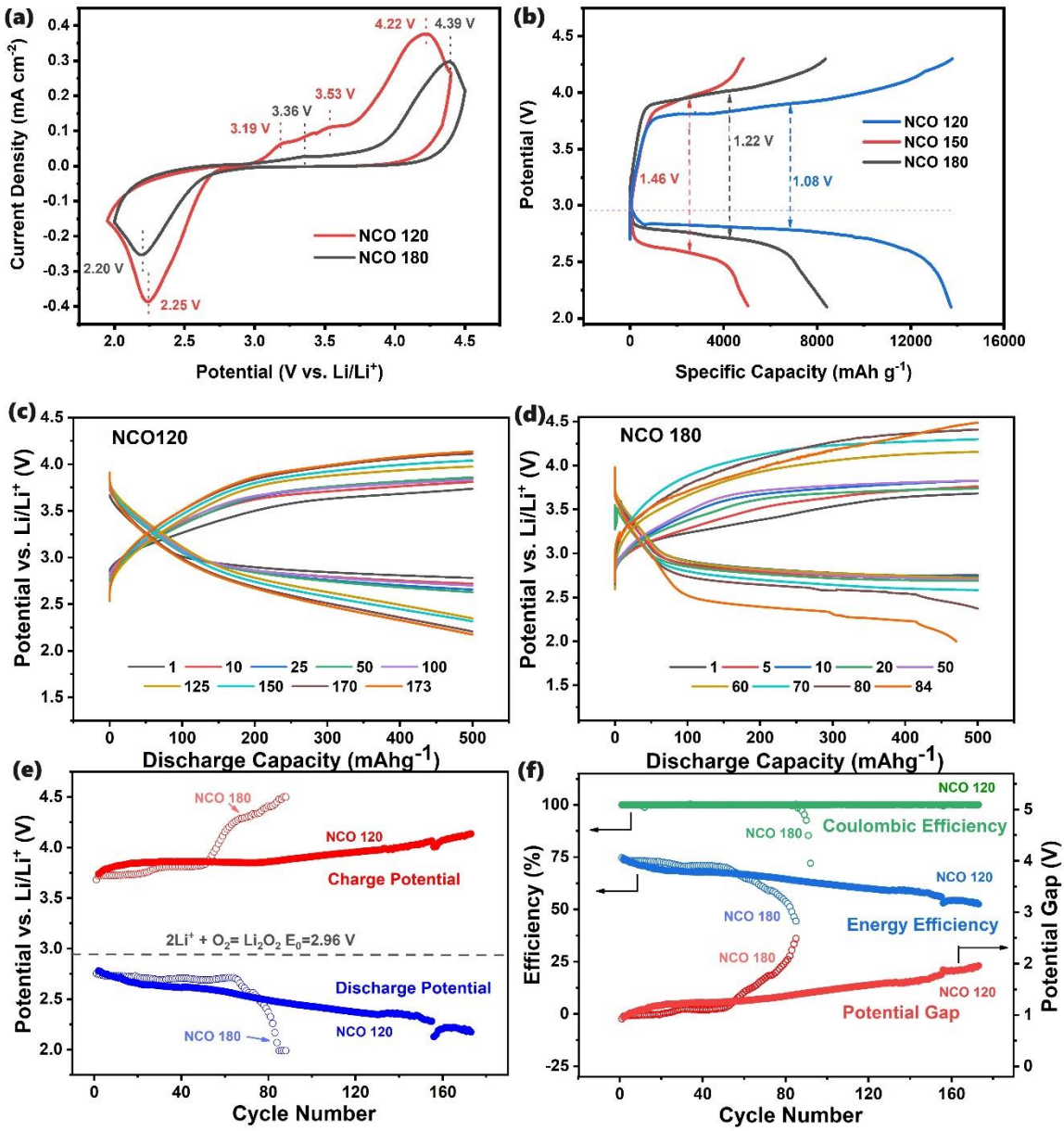

Figure 4: (a) CV analysis @0.2 mVs^{-1} and (b) full discharge-charge @100 mA g^{-1}, and selected discharge-charge curves of (c) NCO120, (d) NCO 180 cathode-based LABs operated at 100 mAg^{-1} for a limited capacity of 500 mAhg^{-1}, (e, f) Cycle life and performance analysis of LABs with NCO 120 and NCO 180 based cathodes with cut-off discharge capacity of 500 mAh g^{-1} with 1M LiTFSl dissolved in TEGDME electrolyte

Aprotic Li-air battery analysis

Following impressive ORR and OER performances in an aqueous medium, aprotic Li-air batteries were assembled using NCO 120 as the binder-free cathode, Li metal foils, and 1M LiTFSl in TEGDME as the electrolyte. LAB cells with NCO 180 and NCO150 cathodes were also constructed for comparison. The cyclic voltammetric (CV) curves recorded for the LABs in the voltage window of 2.0- 4.5 V at 0.2 mV s^{-1} scan rate are presented in Figure 4 (a). A detailed assessment of CV curves and the associated electrochemical reactions and relevant product characteristics can be found in the supplementary section. In summary, the NCO 120 cathode demonstrates superior performance with more positive ORR peak positions, less positive OER peak positions, and higher current densities. As was explained in the supplementary section, it is noteworthy to mention that the stochiometric changes engineering a favourable surface electronic structure with plentiful unsaturated e_g orbital coordinates could lead to the high adsorption in NCO 120, supporting the formation of well-adsorbed reaction intermediates allowing an easy decomposition of the discharged products which is possibly in weakly crystalline nature. The ability to decompose a higher

portion of Li_2O_2 at a lower overpotential could suppress the amount of singlet oxygen ($^1O_2$) that could be generated during the decomposition of the discharged products at higher potentials, where the singlet oxygen was identified as the main culprit causing parasitic reactions during Li-O_2 battery cycling.[16]

The superior performance of the NCO 120 cathode is further investigated using the charge-discharge profiles of the LABs presented in Figure 4 (b). The discharge capacities of the batteries follow the order of NCO 120> NCO 180> NCO 150, following the same pattern observed during the aqueous medium. The initial discharge capacities of 5079 mAh g^{-1} and 8431 mAh g^{-1} showed by NCO 150 and NCO 180 based LABs, respectively is only 36.9 % and 61.3 % of the specific discharge capacity of 13759 mAh g^{-1} achieved by the NCO 120 cathode-based battery. In addition to the remarkable catalytic activity displayed by NCO 120 owing to the abundant presence of surface catalytic sites featuring unsaturated e_g orbitals as discovered through TEM and XPS studies, the high surface area and interconnected mesoporous microstructure, as evidenced by BET and SEM studies, can also be considered as the main attributes of its superior charge-discharge performance. This is particularly evident in its ability to accommodate a substantial quantity of nanosized Li_2O_2 crystals and amorphous discharge products. The lowest observed charge voltage plateau of 3.89 V and the highest discharge voltage plateau of 2.80 V, along with the minimal charging overpotential of 1.09 V, are distinctive features of the NCO 120-based LAB, confirming the high affinity towards the reaction intermediates. These characteristics further underscore its superior catalytic powers compared to the NCO 150 and NCO 180 microstructures, which exhibit significantly higher overpotentials of 1.46 V and 1.22 V, respectively, with limited support for OER and ORR.

The cyclability of NCO 120 and NC 180 cathode-based LABs was evaluated using the charging and discharging method at a current rate of 100 mA g^{-1} with a limited discharge capacity of 500 $mAhg^{-1}$. Figure 4(c)- (d) presents the resultant charge-discharge curves. The LAB constructed with NCO 120 demonstrated the longest cycle life, successfully working up to 173 continuous cycles. In contrast, LAB with NCO 180 cathode only lasted for 84 cycles. The long cyclability exhibited the stability of the catalyst over a prolonged period. The exhibited excellent cyclability of NCO 120-based LAB also surpasses the performances of many other $NiCo_2O_4$ and related-spinel cathode-based Li-Air and Li-O_2 batteries, as presented in Figure 6(a). [41–45]

In addition to individual charge-discharge curves, the respective potentials at the end of each step were also recorded. As illustrated in Figure 4 (e), the charge potential remains mostly constant at around 3.85 V for the first 80 cycles before it rises gradually. The observation validates the undiminished OER support and the availability of catalyst sites to get attached for the reaction intermediates. The discharge potential, however, dropped steadily throughout the cyclic study until it reached the cut-off potential of 2.0 V during the 173rd cycle for NCO 120. In contrast, the relatively stable charge and discharge potentials rose and dropped sharply, respectively, by the 50th cycle during the cyclability analysis of NCO 180-based LAB, causing a sharp rise in the potential gap, as can be seen in Figure 4(d) and (f). We believe that either the unfavourable physical properties of the NCO 180 cathode, where the attached 2D sheets could lose contact with the surface of the cathode or the fast-decaying catalytic properties are responsible for the reduced activity. Even though the NCO 180-based LAB performed marginally better in the first few cycles, the overall impressive, smooth, and steady operation was observed with the NCO 120-based Li-air battery system during the cyclability analysis, performing 173 cycles in the dry air medium for the span of 3460 hours by maintain a lower potential gap and the full cyclability. Further detailing on characteristic behaviour can be found in the supporting information. The high oxygen, LiO_2, and Li_2O_2 adsorption capabilities in NCO 120-based cathode attributed to its supportive surface electronic structure may contribute to long cyclability and low charge/discharge overpotential by providing high adsorption to the reaction intermediates. Hence, a swift decomposition at lower charging overpotentials was achieved by forming a nano-crystalline layer of $Li_{2-x}O_2$ well-attached at the surface during discharge while suppressing the discharge product, mitigating the electrolyte and the formation of a large toroid of Li_2O_2.

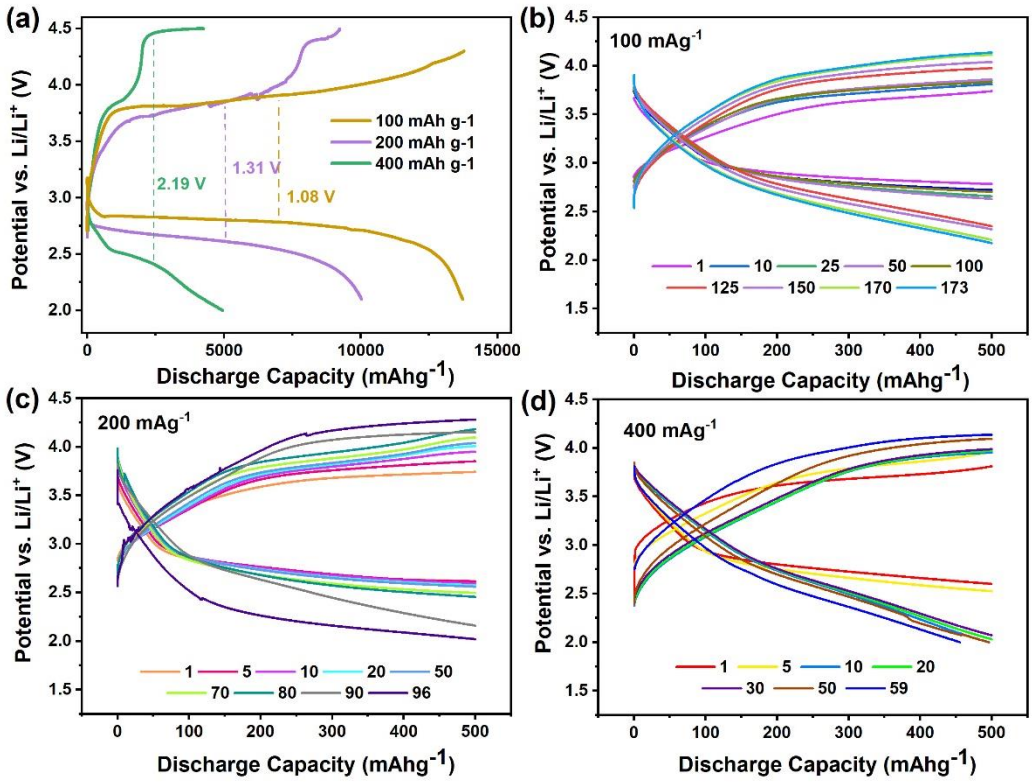

Figure 5: Electrochemical performance analysis of NCO120 cathode-based LABs under different current densities: (a) full discharge-charge capacity, selected discharge-charge curves under a current density of (b) 100 mAg^{-1}, (c) 200 mAg^{-1}, and (d) 400 mAg^{-1}

We then studied the performance of the NCO 120 LAB at higher current ratings. In principle, lower discharge capacities were expected at higher current densities since the discharge product is expected to form a thin layer at the cathode surface, ruling out further discharge by quickly covering all available sites for oxygen adsorption. Further, the decrease in oxygen diffusion depth contributes inversely to achieving higher discharge capacities at higher current densities.[8] As the current density increased to 200 mAg^{-1}, NCO120 LAB showed an impressive discharge capacity of 10030 mAh g^{-1} with a 93% coulombic efficiency, as indicated in Figure 5 (a). This achievement constitutes a noteworthy 72.7% of capacity retained compared to the discharge capacity obtained at a 100 mA g^{-1} current rating. The discharge capacity decreased to 4,945 mAh g^{-1} as the current density was further raised to 400 mAg^{-1}. This change was accompanied by a coulombic efficiency of 84.6% and a charge/discharge overpotential of 2.19 V, underscoring the challenges in maintaining full reversibility after full discharge, thus indicating reduced capacity. The cyclability of the NCO 120 LAB was impressively high at 200 mA g^{-1} and 400 mA g^{-1} current density, operating at nearly 100% coulombic efficiency for 96 and 59 respective cycles, as indicated in Figure 5 (b-d). In addition, the battery lasted for another 16 cycles of operation before decaying its performance <50% of charge retention as the cells cycled at the rate of 400 mA g^{-1}. Further, two voltage plateaus related to fast charging can be found in the studies. This is more likely to be associated with the decomposition of the surface-grown nanocrystals of $Li_{2-x}O_2$ at a lower potential and the large toroid of Li_2O_2 needing a relatively high potential to get decomposed. The presence of the voltage plateaus in a similar potential range as observed as peak positions during the cyclic voltammetric studies further justifies the observations. In addition, a smooth charging step under 100 mAg^{-1} charge rate is noticeable, and it suggests that the formation of nanocrystalline/ amorphous product of $Li_{2-x}O_2$ is favourable during the discharging step. It is noteworthy to mention that the limiting factor for terminating the battery cycling occurred as the discharge process reached its cut-off conditions, unlike the typical scenario of the inability to complete recharge under the effective potential window. Therefore, it could suggest that the catalyst is exhibiting far greater OER

performances over the ORR activity. Restrictions at oxygen diffusion with limited O_2 content in dry air and the changes in the cathode surface/ electrolyte during continuous cycling may trigger the reduction in the discharge potential.

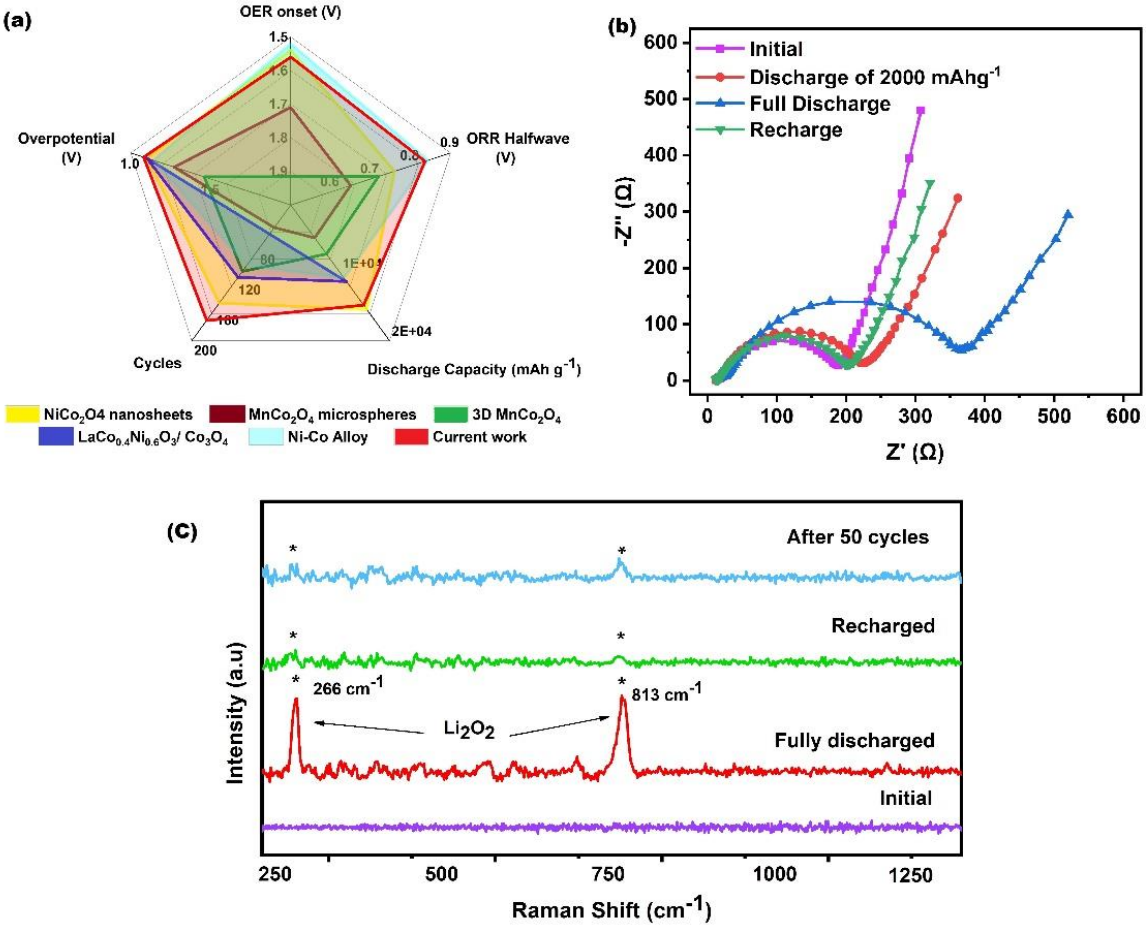

Figure 6: (a) Literature comparison [41–45], (b) EIS analysis, (c) ex-situ Raman analysis on LAB cells with the free-standing NCO 120 cathode at various levels of discharge and charge

Figure 6 (a) compares the NCO 120 electrode and other reported LAB cathodes in the literature. The figure demonstrates the stable and outperforming bifunctional catalytic activities of NCO 120. For instance, a slightly improved OER onset potential and ORR halfwave potential were achieved by Chang et al. [45] with the aid of a hybridized carbonaceous structure, where their Co-Ni alloy was enclosed within N-doped graphene. However, this approach has drawbacks. Specifically, it led to the system's deterioration, reducing the battery's lifespan, as it couldn't endure a significant number of charge/discharge cycles, possibly due to the electrochemical instability of the graphene at higher potentials. This prompted us to delve deeper into the associated reaction mechanism and gain further insights into the exceptional bifunctional catalytic activity of the freestanding NCO cathode. Consequently, we conducted ex-situ analysis of discharge and charge products using Electrochemical Impedance Spectroscopy (EIS), SEM, and Raman spectroscopy.

Since a bottom-up growth approach has been used to grow the NCO catalysts on the Ni foam substrate, a superior interfacial bonding with good ohmic contact in between the catalyst sites and the substrate is expected. EIS analysis was conducted on LAB cells with the freestanding NCO 120 cathode at various levels of discharge, as presented in Figure 6 (b) as the battery discharged/charged at 100 mAh^{-1} current density, using a sinusoidal signal with the amplitude of 5 mV_{pp} in the frequency domain of 0.01 -1000 Hz. In the Randles circuit fitted Nyquist plot obtained for LABs, the high-frequency interception of the semicircle with the real axis is related to the series ohmic resistance (R_s), which is a sum of the lead resistance, contact resistance, and ionic resistance by the electrolyte and the separator, while the semicircle denotes the charge transfer resistance (R_{ct}) at low frequencies. The lowest Rs and Rct with respective values of 11.8 Ω and 168.3 Ω were found initially before the discharge. The ohmic resistance increased to 12.6 Ω, and 16.3 Ω, respectively after being discharged to 2000 mAhg-

[1] depth and discharged fully, before decreasing to 12.2 Ω after being charged back. The charge transfer resistance also followed the same trend, where the respective values of 196.5 Ω, 362.7 Ω, and 177.4 Ω were recorded after the phases of limited discharge (2000 $mAhg^{-1}$), full discharge, and recharge. Irrespective of identified surface defects and favourable electronic structure, the overall insulative characteristics of metal-oxides may have contributed heavily to the initial resistance. An increase in the R_s and R_{ct} during the discharge is associated with the formation of the surface adsorbed Li_2O_2 insulating layer on the cathode, and the increased ionic resistance is also contributed as the Li-ion concentration reduced considerably while it participates in forming non-soluble Li_2O_2. It is noteworthy to mention that the impedance increased only marginally after discharged to 2000 $mAhg^{-1}$, and more importantly, after the first charge, the R_s and R_{ct} reduced substantially, almost reaching the initial conditions, verifying the full decomposition of the discharged product, which further implies the excellent redox kinetics in NCO 120 freestanding cathode-based LAB. Further, the identified remarkable recoverability of the cell after being charged back may be pivotal in demonstrating excellent cycle performances of the NCO 120-based cells.

Raman analysis is a potent technique for analyzing the exiting phases on the air electrode, and it could identify the presence of a range of electrochemically and chemically generated Li species, which affects the cyclability and efficiency of the LAB. The conducted ex-situ Raman analysis on the battery cathode obtained at different stages of the discharge and charge is presented in Figure 6 (c). Apparently, the synthesized starting material is free of Li-related Raman peaks in the area of interest. Upon full discharge, two distinct peaks at 266 and 813 cm-1 arose, which could be assigned to the desired discharge product of Li_2O_2 [46]. The battery's almost full reversibility is demonstrated as the peaks disappear upon charging, where only a slight trace can be identified. Further, the Raman spectrum obtained for the NCO120 cathode after 50 cycles indicates residue Li_2O_2 left at the cathode surface. This explains the loss of capacity as more undecomposed discharge products accumulate at the cathode surface as the cycle number progresses. In addition to reversibility, the results further verify that none of the parasite products, like Li_2CO_3 or LiOH, were formed in the system in detectable quantities. High contributions from the self-standing cathode architecture and the high OER activity of the NCO 120 catalyst may pave the path towards a longer life span by minimizing the early degradation of cathode materials and electrolytes. The detection of strong peaks and the respective peak positioning further indicates the formation of amorphous layers of Li_2O_2 over crystalline toroidal-shaped particles since amorphous Li_2O_2 is easily detectable at relatively higher frequencies [42] (than crystalline Li_2O_2) due to its marginally uncoordinated defective nature and shorter O-O bond length.

The conducted ex-situ SEM analysis of the NCO 120 cathode material at various stages of the discharge-charge process also provides further insight into the discharge mechanism, as presented in Figure S10. It was evident that the discharged product fully covered the cathode surface as the battery was fully discharged, as indicated in Figure S10 (b, e), compared to the cathode before discharge as in Figure S10 (a, c). The reversibility of the process is proven as the formed Li_2O_2 was decomposed upon charging, leaving the morphological features of the charged cathode (Figure 9 (c, f)) much similar to the initial NCO 120 cathode as indicated in Figure S9 (a, c). Further, it is noteworthy that the discharged product was deposited over the surface of the cathode as an amorphous coating without any crystalline shape, well distributed along the cathode surface. The observations made here validate the previous observations made during the cyclic voltammetry, galvanostatic charge-discharge, and Raman microscopic analysis, which favours the growth of nanocrystalline/ amorphous discharge product over the growth of toroidal-shaped crystals of Li2O2, especially during the current rate of 100 mAg^{-1}. The high abundance of catalytic sites throughout the cathode surface and the identified superior catalytic activity of the stoichiometrically modified Ni-Co oxide catalyst material with the vacant d-orbital sites with easy accessibility for the charge/ discharge intermediates are expected to favour the growth of easily decomposable surface-attached discharge product, promoting superior LAB performance.

Considering the observations made via EIS, ex-situ Raman, and ex-situ SEM studies, the following mechanism presented in Figure S11 is well suited for describing the discharging-charging process of the studied NCO 120 cathode-based LABs. As the battery discharged, a thin layer of discharge product gradually covered the voids in proximity, and this layer largely dissipated as the battery underwent recharging. Despite earlier conjectures about the passivation of Li-air battery cathodes due to the formation of a thin layer of discharge product on the surface, limiting the discharge capacity, our current study challenges this notion. We achieved a substantial discharge capacity while generating surface adsorbed LiO_2 and Li_2O_2. To attain such a substantial surface coating of the discharge product and to achieve long endurance during cycling, we postulate the following,

1. The defect-rich cathode facets have a supportive electronic structure, promoting fast

adsorption of reaction intermediates, which encourages discharge products to stay intact on the cathode surface even though a solvent with a high donor number (DN) was used. The reaction mechanism for the electrochemical reduction of O_2 occurred at the air-electrolyte-catalyst three-phase interface could be denoted as,

$$Li^+_{(s)} + O_{2(g)} + e \rightarrow LiO_{2(ads)} \quad (1)$$

, where the formed superoxide radical ($O_2^{-\cdot}$) reacts with Li^+ forming LiO_2. Since the produced Lithium superoxide stayed intact with the electrode surface, it could be assumed that the final discharged product of Li_2O_2 was mostly produced by the second electron transfer (as previously introduced) over the disproportionation of LiO_2.

$$Li^+_{(s)} + LiO_{2(ads)} + e \rightarrow Li_2O_{2(ads)} \quad (2)$$

2. The coated discharged product is amorphous and is permeable to Li+ diffusion, allowing further discharge.
3. The catalyst exhibits high OER activity owing to the presence of unsaturated, e.g., orbital coordination sites. The Li_2O_2 is relatively conductive and easily decomposable, enabling a stable LAB operation over 170 cycles with a low charging overpotential.
4. Since the side products, such as Li_2CO_3, were not detected in substantial quantities during the study, it could be assumed that the reversible operation of LAB cells took place without many obstacles related to parasitic reactions due to the following.
    a. As the reduced reactive oxygen species, LiO_2, and Li_2O_2, mostly stayed intact with the surface of the catalysts, it could be assumed that the electrolyte was less exposed to parasitic reactions during the discharging involving possible nucleophilic substitutions and H atom abstractions by the mentioned species.
    b. Since Li_2O_2 stayed intact on the electrode surface as an amorphous coating and since it was fast decomposed upon charging, it could suppress the extensive singlet oxygen generation, protecting the electrolyte from prolonged exposure.
    c. The self-standing NCO 120 cathode remained resistant to parasitic reactions, unlike carbon-based electrodes, which were reported to be susceptible.
    d. The presence of a small CO_2 quantity (~0.04%) in dry air does not seriously affect the reversibility of LAB cells, and the number of parasitic reactions could occur in air medium via generating highly reactive protonated reduced oxygen species as HOO*, HOO^-, and HO* were substantially reduced as the main proton source (moisture) was removed from the medium.

Only providing limited details on surface facets and their adsorption energies could be found as a limitation of the study, which could have a significant correlation with battery performance and be worth investing in the future. Even though we used Ni-Co oxides to demonstrate the effect of stoichiometry on catalytic performances, the concept can be expanded to other systems with greater effectiveness in the future. Since a more sensible pathway towards achieving a true Li-air battery through solid-electrolyte, separating Li metallic anode from the environment, it is particularly important to understand the effectiveness of derived solid electrocatalysts with solid electrolytes and the associated electrochemistry, where the solution-based redox mediators cannot expect to be compatible.

5. Conclusion

In summary, we developed a series of Ni and Co binary oxides with unique hierarchical 3D structures by controlling nucleation and growth during hydrothermal processes. The stoichiometry, electronic properties, morphology, and distortions in the crystal structure of the derived structures were found to depend on the parameters of the synthesis process, yielding three distinctive structures. The material analysis suggested that the NCO 120 has the most favourable catalytic structure with plentiful unsaturated eg orbital coordinates formed through substitutional disorders and a well-formed hierarchical network. This electrode demonstrated exceptional performance, achieving a discharge capacity of 13,759 $mAhg^{-1}$ at a current density of 100 mAg^{-1}. Moreover, the cell operated continuously for 3,460 hours, completing 173 charge/discharge cycles while maintaining a capacity of over 98% coulombic efficiency in a dry-air environment. This performance surpasses the performances of the constructed LABs with NCO 150 and NCO 180, and the performances of many other LABs reported with spinel oxides, indicating the significance of the study. Even though the study used the spinel structures of Ni-Co oxide, the discussed strategy could be extended to optimize the stoichiometric ratios in other similar structures of oxides, sulfides, phosphides,

etc. The introduced highly efficient cathode catalytic system could be coupled with a solid electrolyte to develop long-durable Li-air battery systems in future research by protecting the battery anode against contaminants.

CRediT authorship contribution statement

Shadeepa karunarathne: Conceptualization, Methodology, Investigation, Formal analysis, Visualization, Writing – original draft. **Yasun Y. Kannangara:** investigation, visualization. **Chirag R. Ratwani:** Investigation, Visualization, Writing – review & editing. **Chanaka Sandaruwan:** Investigation, Visualization. **W.P.S.L. Wijesinghe:** Investigation, Visualization. **Ali Reza Kamali:** Resources, Supervision, Funding acquisition, Conceptualization, Writing – review & editing. **Amr M. Abdelkader:** Resources, Supervision, Funding acquisition, Conceptualization, Writing – review & editing.

Conflict of interest

The authors declare no conflict of interest.

References

1 J. F. Mercure, P. Salas, P. Vercoulen, G. Semieniuk, A. Lam, H. Pollitt, P. B. Holden, N. Vakilifard, U. Chewpreecha, N. R. Edwards and J. E. Vinuales, *Nature Energy 2021 6:12*, 2021, **6**, 1133–1143.

2 L. Kong, Z. Li, W. Zhu, C. R. Ratwani, N. Fernando, S. Karunarathne, Amr. M. Abdelkader, A. R. Kamali and Z. Shi, *J Colloid Interface Sci*, 2023, **640**, 1080–1088.

3 M. Salado and E. Lizundia, *Mater Today Energy*, 2022, **28**, 101064.

4 Z. Luo, C. Ji, L. Yin, G. Zhu, B. B. Xu, Y. Wang, T. X. Liu, X. Zhuge and K. Luo, *Mater Today Energy*, 2020, **18**, 100559.

5 L. N. Song, W. Zhang, Y. Wang, X. Ge, L. C. Zou, H. F. Wang, X. X. Wang, Q. C. Liu, F. Li and J. J. Xu, *Nature Communications 2020 11:1*, 2020, **11**, 1–11.

6 N. Imanishi and O. Yamamoto, *Mater Today Adv*, 2019, **4**, 100031.

7 G. A. Attard, P. G. Bruce, E. J. Calvo, Y. Chen, L. A. Curtiss, D. Dewar, J. H. J. Ellison, J. Fernández-Vidal, S. A. Freunberger, X. Gao, C. P. Grey, L. J. Hardwick, G. Horwitz, J. Janek, L. R. Johnson, E. Jónsson, S. Karunarathne, S. Matsuda, S. Menkin, S. Mondal, S. Nakanishi, N. Ortiz-Vitoriano, Z. Peng, J. P. Rivera, I. Temprano, K. Uosaki, E. D. Wachsman, Y. Wu and S. Ye, *Faraday Discuss*, 2024, **248**, 210–249.

8 S. Hyun, B. Son, H. Kim, J. Sanetuntikul and S. Shanmugam, *Appl Catal B*, 2020, **263**, 118283.

9 I. V. Zenyuk, P. K. Das and A. Z. Weber, *J Electrochem Soc*, 2016, **163**, F691.

10 C. R. Ratwani, S. Karunarathne, A. R. Kamali and A. M. Abdelkader, *ACS Appl Mater Interfaces*, 2024, **16**, 5, 5847–5856.

11 *Nature Catalysis 2019 2:9*, 2019, **2**, 735–735.

12 J. H. Kim, A. G. Kannan, H. S. Woo, D. G. Jin, W. Kim, K. Ryu and D. W. Kim, *J Mater Chem A Mater*, 2015, **3**, 18456–18465.

13 C. K. Lee and Y. J. Park, *Nanoscale Res Lett*, 2015, **10**, 319.

14 P. Sennu, M. Christy, V. Aravindan, Y. G. Lee, K. S. Nahm and Y. S. Lee, *Chem. Mater.* 2015, **27**, 16, 5726–5735.

15 B. M. Gallant, R. R. Mitchell, D. G. Kwabi, J. Zhou, L. Zuin, C. V Thompson and Y. Shao-Horn, *The Journal of Physical Chemistry C*, 2012, **116**, 20800–20805.

16 N. Mahne, B. Schafzahl, C. Leypold, M. Leypold, S. Grumm, A. Leitgeb, G. A. Strohmeier, M. Wilkening, O. Fontaine, D. Kramer, C. Slugovc, S. M. Borisov and S. A. Freunberger, *Nat Energy*, 2017, **2**, 17036.

17 H. Osgood, S. V. Devaguptapu, H. Xu, J. Cho and G. Wu, *Nano Today*, 2016, **11**, 601–625.

18 T. Şener, E. Kayhan, M. Sevim and Ö. Metin, *J Power Sources*, 2015,**288**, 36-41.

19 H. Hu, Y. Meng, Y. Mei, P. X. Hou, C. Liu, H. M. Cheng, M. Shao and J. C. Li, *Energy Storage Mater*, 2023, **54**, 517–523.

20 P. Moni, S. Hyun, A. Vignesh and S. Shanmugam, *Chemical Communications*, 2017, **53**, 7836–7839.

21 J. Wang, R. Zhan, Y. Fu, H. Y. Yu, C. Jiang, T. H. Zhang, C. Zhang, J. Yao, J. F. Li, X. Li, J. H. Tian

and R. Yang, *Mater Today Energy*, 2017, **5**, 214–221.

22 C. V Amanchukwu, J. R. Harding, Y. Shao-Horn and P. T. Hammond, *Chemistry of Materials*, 2015, **27**, 550–561.

23 J. Yuan, Z. Liu, Y. Wen, H. Hu, Y. Zhu and V. Thangadurai, *Ionics (Kiel)*, 2019, **25**, 1669–1677.

24 B. Sun, P. Munroe and G. Wang, *Scientific Reports 2013 3:1*, 2013, **3**, 1–7.

25 L. Ren, R. Zheng, D. Du, Y. Yan, M. He, Z. Ran, M. Li and C. Shu, *Chemical Engineering Journal*, 2022, **430**, 132977.

26 N. C. Lai, G. Cong, Z. Liang and Y. C. Lu, *Joule*, 2018, **2**, 1511–1521.

27 Z. Zhou, L. Zhao, J. Wang, Y. Zhang, Y. Li, S. Shoukat, X. Han, Y. Long and Y. Liu, *Small*, 2023, **19**, 2302598.

28 X. Shi, S. L. Bernasek and A. Selloni, *The Journal of Physical Chemistry C*, 2017, **121**, 3929–3937.

29 K. Bakken, O. G. Grendal and M. A. Einarsrud, *J Solgel Sci Technol*, 2023, **105**, 596–605.

30 G. E. Park, H. T. T. Le, H. S. Kim, P. N. Didwal and C. J. Park, *Ceram Int*, **2020**, 12,46.

31 L. Cai, Y. Li, X. Xiao and Y. Wang, *Ionics (Kiel)*, 2017, **23**, 2457–2463.

32 Z. Yan, D. A. Keller, K. J. Rietwyk, H.-N. Barad, K. Majhi, A. Ginsburg, A. Y. Anderson and A. Zaban, *Energy Technology*, 2016, **4**, 809–815.

33 T.-C. Chang, Y.-T. Lu, C.-H. Lee, J. K. Gupta, L. J. Hardwick, C.-C. Hu and H.-Y. T. Chen, *ACS Omega*, 2021, **6**, 9692–9699.

34 S. V Devaguptapu, S. Hwang, S. Karakalos, S. Zhao, S. Gupta, D. Su, H. Xu and G. Wu, *ACS Appl Mater Interfaces*, 2017, **9**, 44567–44578.

35 M. Sun, S. Guo, Z. Wang, L. Zou, B. Chi, J. Pu and J. Li, *Electrochim Acta*, 2020, **363**, 137235.

36 T. H. Ko, K. Devarayan, M. K. Seo, H. Y. Kim and B. S. Kim, *Scientific Reports 2016 6:1*, 2016, **6**, 1–9.

37 W. Zhang, H. Shen, M. Yin, L. Lu, B. Xu and D. Li, *ACS Omega* 2022, **7**, 19, 16494–16501.

38 Y. Y. Kannangara, S. Karunarathne, W. P. S. L. Wijesinghe, C. Sandaruwan, C. R. Ratwani, A. R. Kamali and A. M. Abdelkader, *J Energy Storage*, 2024, **84**, 110717.

39 K. L. Bao, J. Y. Xu, N. F. Yu, J. B. Kuang, Z. T. Yang, H. Chen, J. L. Ye and Y. P. Wu, *Energy and Fuels*, 2022, **36**, 6542–6551.

40 C. C. Li, W. Zhang, H. Ang, H. Yu, B. Y. Xia, X. Wang, Y. H. Yang, Y. Zhao, H. H. Hng and Q. Yan, *J Mater Chem A Mater*, 2014, **2**, 10676–10681.

41 X. Guo, J. Zhang, Y. Zhao, B. Sun, H. Liu and G. Wang, *ACS Appl Energy Mater*, 2019, **2**, 4215–4223.

42 S. Ma, L. Sun, L. Cong, X. Gao, C. Yao, X. Guo, L. Tai, P. Mei, Y. Zeng, H. Xie and R. Wang, *Journal of Physical Chemistry C*, 2013, **117**, 25890–25897.

43 Z. Li, Y. Lv, Y. Yu, J. Yin, K. Song, B. Yang, L. Yuan and X. Hu, *J Alloys Compd*, 2020, **817**, 152736.

44 M. Sun, S. Guo, Z. Wang, L. Zou, B. Chi, J. Pu and J. Li, *Electrochim Acta*, 2020, **363**, 137235.

45 Z. Chang, F. Yu, Z. Liu, S. Peng, M. Guan, X. Shen, S. Zhao, N. Liu, Y. Wu and Y. Chen, *ACS Appl Mater Interfaces*, 2020, **12**, 4366–4372.

46 F. S. Gittleson, K. C. Yao, D. Kwabi,] Sayed, Y. Sayed, W.-H. Ryu, Y. Shao-Horn and A. D. Taylor, *ChemElectroChem,* 2015, ***2***, 1446.